



High-resolution simulation of air-breathing rotating detonation engines

Han Peng¹, Ralf Deiterding²,

Abstract

Rotating detonation engines (RDEs) use one or multiple spinning detonations to burn propellants in an annular combustion chamber. RDEs are of great interest for hypersonic propulsion as detonation combustion involves a gain in total pressure. Yet, the complex energetic interplay between the leading shock wave and the combustion front in a detonation wave and its propagation speed of around 2000 m/s make the experimental investigation of RDEs quite challenging. Numerical simulations are therefore of crucial importance for predicting stable RDE operation at the design stage. Here, we conduct predictive 3D numerical simulations of non-premixed detonation combustion in RDEs using our parallel bock-structured finite volume adaptive mesh refinement framework AMROC, which solves the thermally perfect multi-component Navier-Stokes equations with a detailed chemical model as governing equations on body-fitted curvilinear meshes with dynamic mesh adapation following the detonation fronts. After validating the methodology for a hydrogen-air RDE with available experimental data, we implement constant temperature wall boundary conditions and demonstrate that the number of detonation waves remains unchanged, and that the average detonation velocity deficit rises only slightly, confirming that RDEs can be cooled considerably without significantly affecting the detonation efficiency. Finally, we present simulations with different back pressures of a cooled prototype RDE combustion chamber intended for a laboratory turbine engine running on ethylene and air. The ethylene-air simulations demonstrate that despite a considerably reduced detonation velocity in this very realistic configuration, gains in total pressure at the outlet of 13.3% and 18.1% can still be measured, which demonstrates the benefit of the RDE concept for turbine engines quite clearly.

Keywords: Rotating detonation engine, pressure gain combustion, numerical simulation, curvilinear meshes, adaptive mesh refinement

1. Introduction

Rotating detonation engines (RDEs) are a type of engine that use one or multiple detonations to compress and burn fuel in a disk- or cylindrical-shaped device. RDEs have been considered as a potential replacement for current jet engine systems since they promise pressure-gain combustion and hence could be more efficient than conventional pressure-constant combustion [1]. RDEs can also operate over a wide range of speeds and pressures, which makes them attractive for use in aerospace propulsion [2]. However, the formation of detonation waves in the annular combustor is a complex, highly nonlinear phenomenon and influenced by a large number of parameters. Also the heat release in the confined annular combustion chamber poses significant challenges for thermal management [3]. Further research is required to optimize the cooling systems of RDEs in preparation for future long-duration tests.

Although many experimental studies have been carried out on different aspects of RDEs, including the detailed extensions of the annular combustion chamber, the conditions of propellant injection, the effects of fuel and oxidizer mixing processes, improving the specific impulse when used as a rocket engine and the application in turbojet engines, to name just a few, no reliable analytic model exists that would predict the detailed detonation behaviour and hence combustion chamber performance. Numerical simulations provide a means to study RDE combustion in detail, however they also face

¹School of Aerospace Engineering, Xiamen University, han.peng@xmu.edu.cn

²Department of Aeronautics & Astronautics, University of Southampton, r.deiterding@soton.ac.uk

various challenges. While early RDE studies were inviscid, two-dimensional and used simplified chemical models, they lacked the ability to correctly simulate the variety of conditions that occur in realistic non-premixed injection processes. In recent years, the field of rotating detonation simulation has seen considerable advancements and it is now generally accepted that predictive RDE simulations need to be three-dimensional and solve the Navier-Stokes equations with full chemistry models [4]. Most 3D numerical models of RDEs also assume adiabatic walls, despite the fact that RDEs typically operate for only a few seconds in experiments and long-duration runs will require wall cooling.

An effective approach to lower the significant computational costs of 3D RDE simulations is the application of adaptive mesh refinement, which allows concentrating the computational efforts at the detonation fronts. Here we briefly describe in Section 2 the inner workings of a body-fitted curvilinear mesh solver [5] within our block-structured adaptive mesh refinement framework AMROC [6] that is particularly suitable for 3D RDE simulations [7]. We then use our solver to study a realistic non-premixed RDE setup running on hydrogen and air that has been experimentally investigated at the US Air Force Research Laboratory [8]. After verification and validation in Section 3, we study the influence of cooled, isothermal wall boundaries on this setup in Section 4.1. In Section 4.2, rotating detonation combustion in ethylene and air is studied in a prototype combustion chamber to be used in a high-pressure turbine. This prototype setup also uses isothermal walls and total pressure gain at the outlet as well as the heat flux at the chamber walls are evaluated. Conclusions are drawn in Section 5.

2. Computational methodology

2.1. Governing equations

The multi-component Navier-Stokes equations with a detailed chemical model are solved as governing equations. They read

$$\partial_{t}(\rho \mathbf{Y}) + \nabla \cdot (\rho \mathbf{u} \mathbf{Y}) - \nabla \cdot \mathbf{j} = \dot{\omega},
\partial_{t}(\rho \mathbf{u}) + \nabla \cdot (\rho \mathbf{u} \mathbf{u} + p \mathbf{I}) - \nabla \cdot \boldsymbol{\tau} = 0,
\partial_{t}(\rho E) + \nabla \cdot (\rho \mathbf{u}(E + p/\rho)) - \nabla \cdot (\mathbf{q} + \mathbf{u} \cdot \boldsymbol{\tau}) = 0,$$
(1)

where \boldsymbol{Y} is the vector of species mass fractions. The total density is computed from the species conservation: $\rho = \sum_{i=1}^{N_{sp}} \rho Y_i$, and N_{sp} is the total number of species. \boldsymbol{u} is the velocity vector of N_D dimensions, and $\dot{\boldsymbol{\omega}}$ is the vector of species production rates. p is the pressure, \boldsymbol{I} is the $N_D \times N_D$ identity matrix, and E is the total specific energy. The multi-species ideal gas state equation

$$p = \sum_{i=1}^{N_{sp}} \rho_i T R_{\mathsf{u}} / W_i \tag{2}$$

is used to close system (1). The species diffusion fluxes j are computed by Fick's law. X is the vector of species mole fractions, and D is the vector of the mixture-averaged diffusion coefficients. The viscous stress tensor τ is calculated using Newton's law, and μ is the dynamic viscosity. The heat-flux vector is modelled using Fourier's law, and κ is the thermal conductivity. The viscous flux terms read

$$j = \rho \mathbf{Y} \mathbf{D}(\nabla \mathbf{X} + (\mathbf{X} - \mathbf{Y}) \nabla p/p) / \mathbf{X},$$

$$\boldsymbol{\tau} = -\frac{2}{3} \mu (\nabla \cdot \boldsymbol{u}) \mathbf{I} + \mu \left[\nabla \boldsymbol{u} + (\nabla \boldsymbol{u})^T \right],$$

$$\mathbf{q} = \kappa \nabla T + \sum_{i=1}^{N_{sp}} h_i j_i.$$
(3)

The total specific energy in (1) can be computed by

$$E = \sum_{i=1}^{N_{sp}} Y_i \left(h_{\text{ref}}^0 + \int_{T_{\text{ref}}}^T c_{\mathbf{p}_i} dT \right) - \frac{p}{\rho} + \frac{1}{2} u^2.$$
 (4)

The constant pressure specific heat $c_{\mathbf{p}_i}(T)$ is dependent on temperature. It is firstly calculated by the polynomial functions in the CHEMKIN II library [9], and then a linear tabulation method is used to accelerate the evaluation [10].

The species production rates in (1) are calculated by a chemical reaction mechanism of J steps as

$$\dot{\omega}_{i} = \sum_{j=1}^{J} \left(\nu_{ji}^{r} - \nu_{ji}^{f} \right) \left[k_{j}^{f} \prod_{n=1}^{N_{\text{sp}}} \left(\frac{\rho_{n}}{W_{n}} \right)^{\nu_{jn}^{f}} - k_{j}^{r} \prod_{n=1}^{N_{\text{sp}}} \left(\frac{\rho_{n}}{W_{n}} \right)^{\nu_{jn}^{r}} \right], i = 1, \dots N_{\text{sp}}.$$
 (5)

The rate constant of forward and reverse chemical reaction is given by the Arrhenius formula

$$k_j^{f/r}(T) = A_j^{f/r} T^{\beta_j^{f/r}} \exp\left(-\frac{E_j^{f/r}}{RT}\right),\tag{6}$$

where $A_j^{f/r}$ is the pre-exponential factor, $\beta_j^{f/r}$ is temperature exponent, and $E_j^{f/r}$ is the activation energy of the reaction. The three Arrhenius coefficients are given by the chemistry mechanism files. In reversible reactions, the reverse chemical reaction rate constant is calculated from the equilibrium constant.

2.2. Finite volume schemes

The HLLC (Harten-Lax-van leer contact) scheme is implemented to approximate the inviscid fluxes. Facet-dependent rotation matrices are used to rotate the velocities in the discrete state vector Q aligning with the grid for the 3D curvilinear grid,

$$\tilde{F}_{i+\frac{1}{2},j,k}^{n} = T_{\mathsf{s}}^{-1} F\left(T_{\mathsf{s}} Q_{i+\frac{1}{2},j,k}^{\mathsf{n},\mathsf{l}}, T_{\mathsf{s}} Q_{i+\frac{1}{2},j,k}^{\mathsf{n},\mathsf{r}}\right). \tag{7}$$

After computing the numerical flux function F by the HLLC approximate Riemann solver, the inverse matrix $T_{\rm s}^{-1}$ is employed to rotate the numerical flux back to the Cartesian coordinate system in physical space. The viscous fluxes on curvilinear meshes are calculated at each face in physical space through a coordinate transformation. When evaluating the CFL (Courant-Friedrichs-Lewy) condition, the effects of both inviscid and viscous fluxes is considered. The global CFL number is defined as the maximum value across the three spatial dimensions and is evaluated for the whole system (1). The subsequent global time step is computed based on the CFL number from the previous time step and a user-defined target CFL number. Given the method's strictly explicit nature, a target CFL number less than 1 is applied across all cases.

The Strang operator splitting approach is employed for temporal discretization, which separates different physical processes into fractional steps and enables the use of different schemes for them. For the nonstiff flux terms, a second-order central difference method is used for viscous fluxes discretization. The second-order MUSCL-Hancock method is used to reconstruct the inviscid fluxes and also advance the time. For the 3D curvilinear grids, the variables Q in the physical space are transformed to computational space Q = JQ by using the Jacobian determinant of the grid $J = \det |\partial (x,y,z) / \partial (\xi,\eta,\zeta)|$. After the reconstruction, the variables are transformed back to the physical space and are integrated by half a time step before being used for the flux estimation in the HLLC solver. For the stiff source terms, a semi-implicit generalised Runge–Kutta method of fourth order (GRK4A) is adopted to integrate the chemical kinetics, cf. [10].

2.3. Adaptive mesh refinement

AMROC [6] adopts a patch-wise refinement strategy, where the entire domain comprises a collection of blocks. Within these blocks, cells are dynamically flagged using specified refinement criteria. The flagged cells are subsequently grouped into a region of variously sized rectangular blocks. Once the refined cells are created from their parents, a hierarchy of embedded grid patches with multiple levels is established, cf. [6].

In AMROC, the finite volume integrator implementation is effectively separated from the adaptive strategy [6]. The numerical schemes are employed simultaneously on grids at different levels. In addition

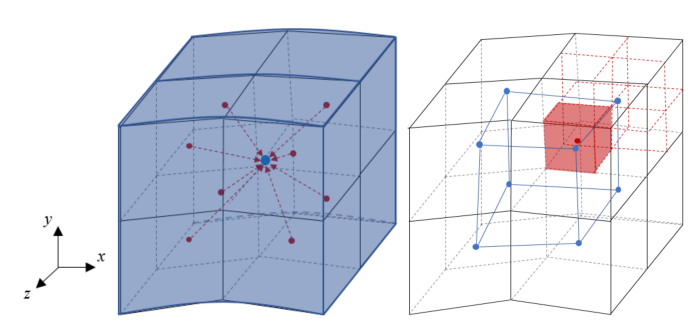


Fig 1. Schematic of the restriction (left) and prolongation (right) operations.

to the Cartesian mesh, a curvilinear structured mesh can also be applied to the entire SAMR technique since the structured topology and internal data layout in AMROC is fully preserved. For instance, to generate the coordinates of grids at a higher level (l+1) or a lower level (l-1), the coordinates of the flagged uniform Cartesian mesh in computational space at level l are refined or coarsened, respectively. By using the same transformation function on each level, the new coordinates in computational space $(\xi_{l\pm 1},\eta_{l\pm 1},\zeta_{l\pm 1})$ are used to generate curvilinear structured grids in physical space $(x_{l\pm 1},y_{l\pm 1},z_{l\pm 1})$ at the new level.

The transfer between refinement levels also requires routines that consider the geometric mapping. A conservative averaging is used for the fine-to-coarse restriction. Figure 1 depicts an example of the restriction operation between grids on adjacent hierarchy levels with a refinement factor of 2. The restriction strategy is such that the value of the coarse element (displayed by the blue dot) is determined by its n^D (n is the refinement factor and n is the number of dimensions) fine sub-elements (displayed by the red dots) through a conservative average considering the cell volumes.

To illustrate the coarse-to-fine prolongation operation, the locations of the centroid of each cell are also indicated in Fig. 1. A new element is generated by connecting the centroids of each coarse cell. The value in the refined cell can be computed by its closest n^D coarse elements. A trilinear space-interpolation is applied in AMROC to transfer the information from coarse to fine level, which involves a local nonlinear system that is solved by a Newton-Raphson method. If this method is not convergent within given iteration steps, the gradient descent algorithm would be used.

For parallelisation, AMROC implements a rigorous domain decomposition approach in which the workload at higher levels is projected onto distribution units at level 0. Load balanced distribution to processors is achieved through a space-filling curve [6] in computational space. This domain decomposition strategy enhances simulation efficiency and scalability by distributing computation in parallel across multiple processors based on the computational workload required in each region. Continuous redistribution ensures a balanced workload at runtime, particularly as the grids change. The redistribution process occurs at a specified frequency at the base level.

3. Verification and validation

3.1. Numerical configuration

The computational domain of the first 3D annular RDE setup is depicted in Fig. 2. The chamber has an outer diameter of 153.9 mm and a channel width of 7.6 mm, based on one of the experimental configurations in [8] but with some modifications. For simplicity, the plenum and actual injection schemes are not fully represented. The axial height of the chamber is set to 100 mm, and no annular plug nozzle at the chamber outlet is included in the simulation.

The chamber is filled with air at atmospheric pressure and a temperature of 295 K. The presence of nitrogen is assumed as inert. A layer of stoichiometric hydrogen-air mixture is initialised with a height of 10 mm. A region of pure nitrogen and a prescribed 1D ZND detonation solution are used to create a single stable detonation wave in the first cycle. The patch of pure nitrogen usually prevents the formation of a second detonation wave propagating into the reverse direction. Fuel is injected from the

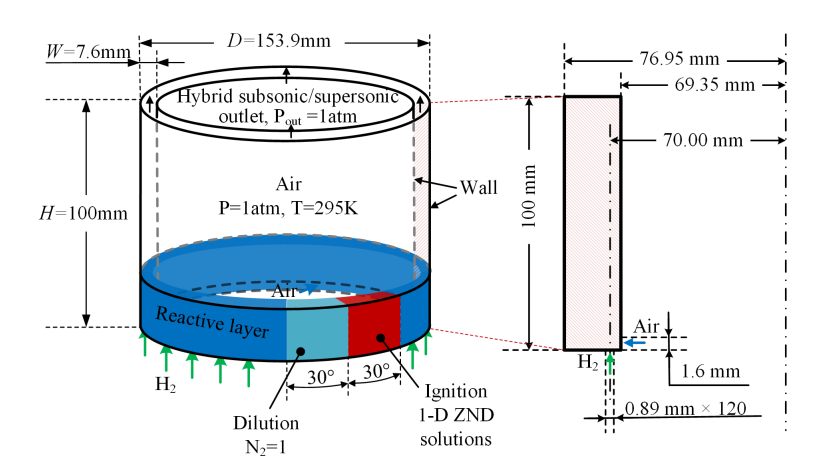


Fig 2. Computational domain of the hydrogen/air annular RDE model.

head plane through 120 holes with a diameter of 0.89 mm and air is injected through a 1.6 mm slit on the inner wall. The hydrogen-air simulations apply the detailed hydrogen reaction mechanism by [11], which uses 9 species and 23 equilibrium reactions.

The 3D annular model's top side is set as a hybrid subsonic/supersonic outflow with atmospheric pressure as ambient pressure. Outflow variables are extrapolated if the local Mach number is greater than 1, otherwise subsonic outlet is set based on ambient pressure. The mass flow inlet is used for both the hydrogen injection holes and the air slit. The total hydrogen mass flow rate is set to $9.3\,\mathrm{g/s}$ and the air mass flow rate is given as $320\,\mathrm{g/s}$, resulting in a globally stoichiometric injection. Other boundaries are considered slip walls, for which either adiabatic wall or isothermal wall boundary conditions are applied in various cases.

The base mesh consists of $20 \times 580 \times 250$ cells and additional refinement levels are applied with a factor of 2 per level. As dynamic refinement criteria scaled gradients of temperature, density and pressure are used. The first four cells near the walls are always flagged to be refined. The target CFL number is set to 0.8. The following simulations were conducted on the high-performance computing cluster Archer-2, where 256 cores (AMD EPYC 7742 2.25 GHz) were used for each case. The total cell number of the two-level grid changes dynamically from 10.4 to 15.5 million. Typical run times for the RDE operating time of 1 ms were approximately 4 to 5 days wall-clock time.

3.2. Mesh dependency study

Three different meshes are tested in the 3D case to study the effects of mesh dependency as presented in Fig. 3. The results demonstrate that the number of waves is independent of the chosen mesh. Table 1 shows the cell count, typical run times for 1 ms operation time, and the detonation velocity comparison in these cases. The detonation velocity is computed on the inner wall through the operation frequency. The results show that the difference in the ratio of detonation velocity to the Chapman-Jouguet (CJ) velocity is within 1% when the mesh is refined. The velocity deficit is 11.4%, 8.7% and 8.1% in these cases, respectively. Despite variations in the flow field when the cell is refined, the two-level mesh is considered a suitable balance between computational accuracy and cost. Hence, the following 3D hydrogen simulations are conducted using this two-level mesh.

3.3. Comparison with experimental results

Figure 4 shows a comparison of the mean static pressure distribution in published experiments [8], simulations [12] and the numerical results obtained by the present solver at different axial positions on the outer wall of the detonation channel. The numerical predictions are in good agreement with the experimental results at a relatively low mass flow rate. The AMROC solver predicts a less fluctuating mean static pressure near the outlet. At the high mass flow rate, this discrepancy is mainly due to the injection simplification on the injectors. In experiments, a large pressure drop is observed in the chamber as an influence of the injector throat.

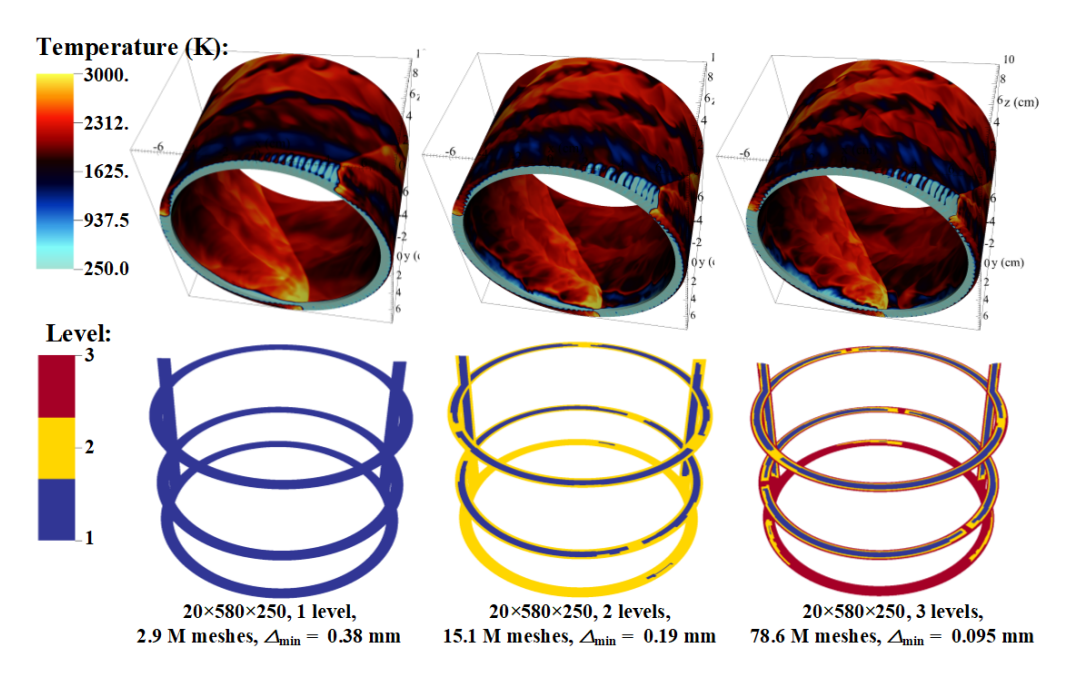


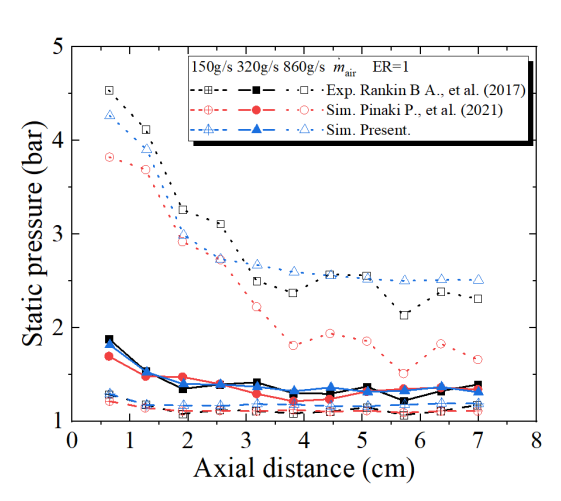
Fig 3. Pseudo-colour images of temperature and refinement levels of the 3D non-premixed hydrogen RDE simulations from Table 1.

Table 1. The hydrogen-air detonation velocity obtained with different mesh resolutions.

Adaptive Level	$\Delta_{\min}(\text{mm})$	Number of cells (M)	Run time (cpu·h)	Detonation velocity (m/s)	Theoretical CJ velocity (m/s)	$%D_{ extsf{CJ}}$
1	0.38	2.9	4260	1751.67		88.6%
2	0.19	\sim 15.1	27648	1803.96	1976.7	91.3%
3	0.095	\sim 78.6	194246	1817.03		91.9%

The respective detonation velocities are also compared as shown in Table 2. The detonation velocity is again computed on the inner wall of the chamber. The simulation overestimates the detonation velocity over 12.6% and 5.3% of the CJ velocity at low mass flow rates, whereas it underestimates the velocity 2.2% at a high mass flow rate, indicating that the errors of simulation are within a reasonable range compared to the experiments. The simulation overestimates the number of detonation heads under different mass flow rates. The number of heads increases with increasing mass flow rate in the simulation.

Several reasons can lead to differences between the experiment and the present simulation. One distinction arises from the simplification of the jet in cross flow configuration, which changes the local mixing near the injection plane. The local numerically enhanced mixing can lead to a bifurcation of detonation heads. Another possible explanation for the discrepancy is that the numerical initiation differs from the experimental ignition. The detonation diffraction at the pre-detonator exit is neglected. This may result in two counter-rotating detonation waves at the initial stage, consuming the mixture ahead of the detonation. Despite the discrepancy from several numerical simplifications, the pressure and detonation velocity are close to the experimental results at an air mass flow rate of $320\,\mathrm{g/s}$. Overall, This configuration is regarded as an acceptable numerical setup for further studies.



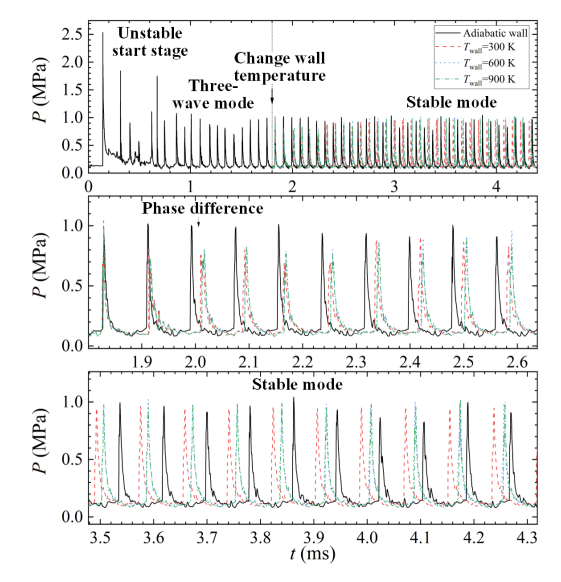


Fig 4. Comparison of measured and predicted mean axial static pressure distribution.

Fig 5. Pressure history in different cases, sensors at $r=73.15\,\mathrm{mm},\ z=5\,\mathrm{mm}$ and $\theta=180^\circ.$

Table 2. Comparison of the hydrogen detonation velocities between the experiment [8] and the present simulations.

Case	Air mass flow rate (g/s)	Number of detonation heads, $n_{\rm det}$	Detonation head height $H_{\text{det}} \times n_{\text{det}}$ (cm)	Detonation velocity (m/s)	Theoretical CJ velocity (m/s)	%D _{CJ}
Experiment	150	1	2.0-2.4	1370	1957.1	70.0%
Simulation	150	2	4.0-4.6	1615.72	1937.1	82.6%
Experiment	320	1	3.8-4.0	1700	1976.7	86.0%
Simulation	320	3	4.5-5.1	1803.96	1970.7	91.3%
Experiment	860	2	5.8-6.2	1690	1965.1	86.0%
Simulation	860	4	6.8-8.0	1647.09	1303.1	83.8%

4. Rotating detonation engines with wall cooling

4.1. Hydrogen-air RDE

We use the RDE setup with 320 g/s from Section 3 with two-level mesh to study the influence on the combustion when a constant temperature is imposed on the inner and outer wall of the annular chamber. We implement this boundary condition by scaling the partial densities ρ_i at the walls by the same factor such that, using the required wall temperature, Eq. (2) at the wall yields an unaltered static pressure. This treatment considers the fact that static pressure across the boundary layer (which is not resolved in our computations) can be assumed to be constant in the wall-normal direction. All the cases start with the adiabatic wall boundary conditions. As shown in Fig. 5, a single detonation wave is ignited at the start, followed by multiple unstable cycles and a transition to a three-wave mode. At $t=1.8\,\mathrm{ms}$, the wall temperature changes in each case. A phase difference appears when isothermal walls are used. In these cases with cooling walls, the pressure peaks drop to around 0.8 MPa and then recover to 1 MPa at the final stable stage. The wave frequency is estimated for the interval [2.3 ms, 4.4 ms] using a fast Fourier transform. The single wave frequency is 4.14, 4.03, 4.03 and 4.05 kHz for the cases with adiabatic walls, and isothermal walls at 300, 600 and 900 K, respectively. Compared to the frequency of 4.3 kHz based on a premixed CJ detonation, the average detonation velocity deficit is 3.7% in the adiabatic case and ranges from 5.8% to 6.3% in the cases with isothermal walls.

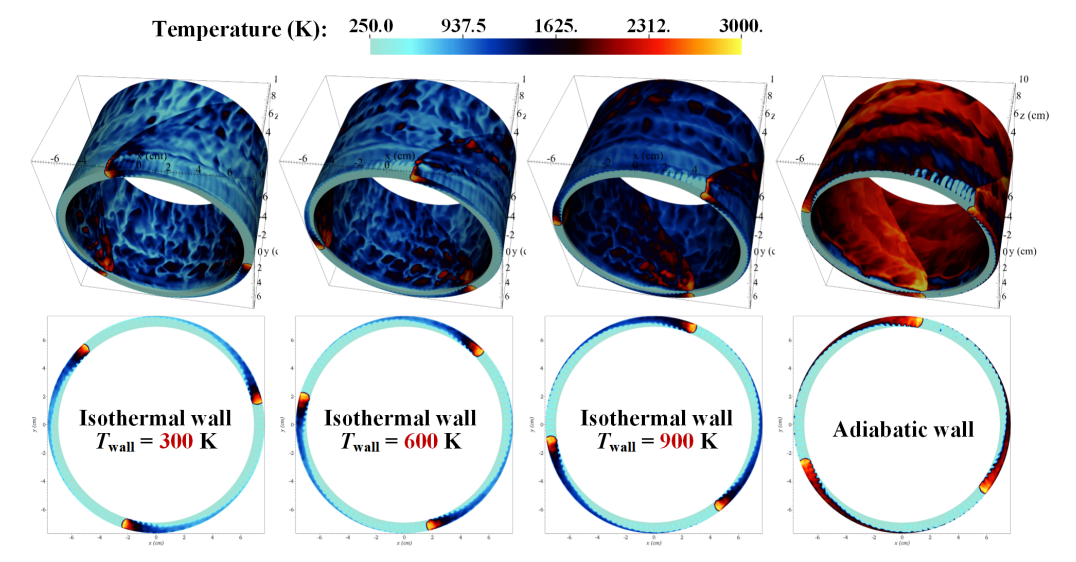


Fig 6. Pseudo-color images of temperature distribution and its slices on the bottom plane.

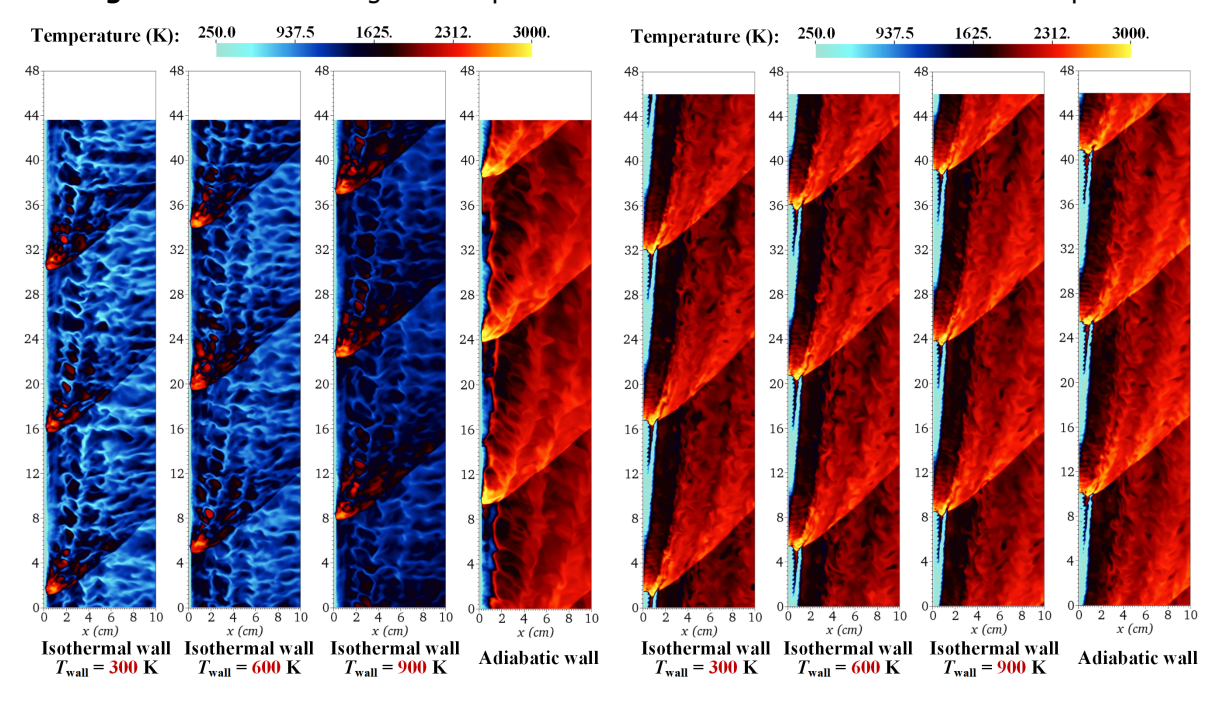


Fig 7. Pseudo-color images of unrolled temperature slices. Left: inner wall. Right: middle of channel.

Figure 6 shows the transient temperature distribution and its slice on the head plane when the different cases run in a stable mode. The use of a cooling wall does not change the number of detonation heads in the present simulations. All the cases still operate in a three-wave mode lasting over 2 ms. The isothermal walls rapidly cool the burned gases, limiting high-temperature regions near the wall to only the area where the detonation exists.

The left-hand side figures of Fig. 7 show the unwrapped slices of the outer wall. In the case using adiabatic walls, the typical rotating detonation structure is observed. The multiple detonation waves are each followed by an oblique shock wave. Irregular slip lines are captured on the contact surface. The fuel-air stratification in the mixture layer is a result of non-premixed injection and incomplete mixing. As the wall temperature decreases, the temperature behind the detonation wave and oblique shock also decreases, but the detonation is still sustained even at a wall temperature of 300 K.

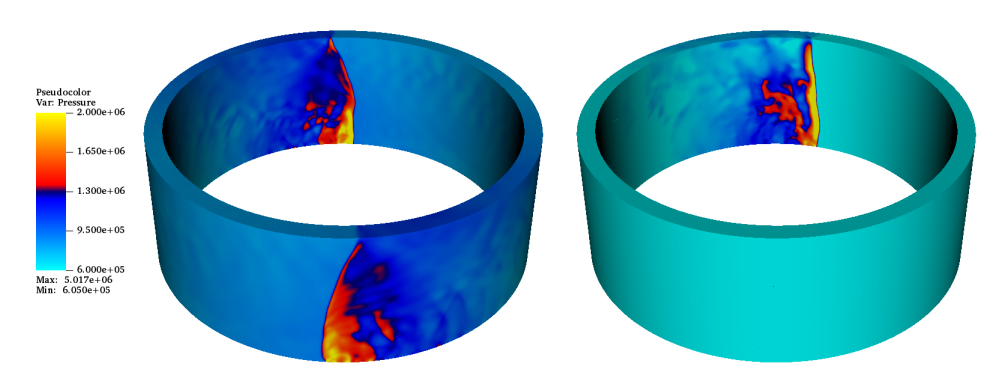


Fig 8. Pressure in ethylene-air RDE. $p_b = 700 \, \text{kPa}$, $t = 7.89 \, \text{ms}$ (left); $p_b = 400 \, \text{kPa}$, $t = 7.78 \, \text{ms}$ (right).

The temperature distribution on the inner wall is depicted in the left-hand side graphics of Fig. 7. The detonation is observed to be detached from the bottom plane due to the presence of the air slit. The height of the mixture layer is seen to be low on the inner wall. Discrete high-temperature regions are also visible behind the detonation wave in the cases with cooling walls. The right-hand side of Fig. 7 presents a comparison of the temperature in the middle of the channel and shows that some parasitic combustion occurs in the mixture layer ahead of the detonation. The differences observed among the cases are entirely minor.

4.2. Ethylene-air RDE

The second configuration is a study of a prototype RDE to be employed as combustion chamber in a small-scale turbine engine. For ease of potential laboratory testing ethylene is used as a fuel. An upstream high-pressure compressor is assumed and in the simulations air as well as ethylene are injected with static temperature 570 K and static pressure 700 kPa. A chamber of middle radius 105 mm and annular chamber width of 10 mm is simulated. An axial chamber height of 80 mm is used. Fully nonpremixed conditions are applied, where the air is injected axially through 90 holes, with their centres equally spaced along the middle radius, and 90 fuel injectors are placed exactly perpendicularly at the outer wall with their centres at a height $z=0.993\,\mathrm{mm}$ above the base plate at z=0. Note that compared to Fig. 2, air and fuel injection location are interchanged. The diameter of the axial air injectors is 5 mm and the diameter of the fuel injectors is 1.324 mm. Both air and fuel are injected with a constant velocity of 200 m/s. Modelling the air simply as a mixture of oxygen and nitrogen of molar ratios 1:3.76, the used injection configuration yields an exactly stoichiometric mixture of ethylene and air in the combustion chamber. Similar to Section 4.1 the annular chamber walls are kept at a constant temperature, which in this case is set to 1000 K, and is imposed already from t=0. The ethylene-air simulations utilize a reduced mechanism for ethylene combustion [13], which employs 10 species and only 10 equilibrium reactions.

We simulate the RDE on a base mesh of $20 \times 800 \times 100$ cells. The initial conditions are similar to those depicted in the left graphic of Fig. 2, where the initial mixture layer is now 30 mm high. A pressure of 500 kPa for the initial chamber conditions and the ZND detonation wave is used. The computations are run again on Archer-2, where now 512 cores (AMD EPYC 7742 2.25 GHz) are applied. The computations are run initially until t=4 ms without dynamic refinement to merely establish stable rotating detonation waves. The computations are then restarted with a second refinement level being allowed and run further until t=8 ms. Like in Fig. 6, static refinement is imposed at the annular chamber walls, however only across a width of a single level-0 cell. Further on, to represent the injection region well, static refinement is enforced for $z\leq 3.2$ mm. Dynamic refinement based on the scaled gradient of pressure is used to track the detonation waves.

Two simulations are presented here and they vary the back pressure that is imposed at the outlet of the annular chamber. In an actual RDE setup the chamber back pressure would be imposed through an annular nozzle, yet the interplay between RDE chamber and a nozzle with converging inlet section

Table 3. Characterization of the ethylene RDEs.

700	400
1.550	1.779
2	1
881.1	572.5
1109.5	1121.6
1859	1850
59.7	60.6
925.7	636.5
817.2	538.8
108.5	97.8
13.3	18.1
	1.550 2 881.1 1109.5 1859 59.7 925.7 817.2 108.5

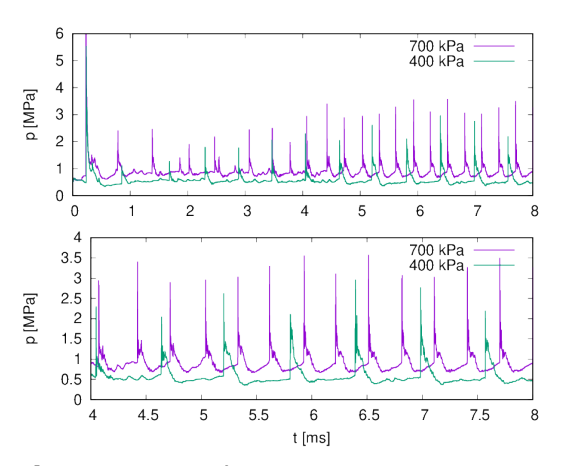


Fig 9. Pressure histories at $r=105\,\mathrm{mm},\ z=5\,\mathrm{mm}$ and $\theta=180^\circ.$

is complex. It is prudent to first establish the range of back pressures at the chamber outlet that an annular nozzle has to provide in which stable rotating detonation waves can actually exist. We compare a case with outlet back pressure of $p_b=700\,\mathrm{kPa}$, which is representative to regular operating conditions, to a case with $p_b=400\,\mathrm{kPa}$, which is close to the limit that allows a rotating detonation wave to be sustained. Two representative time steps at the end of the simulations are displayed in Fig. 8. It is imminent that the lower back pressure has caused the switch to a single detonation wave. Figure 9 displays the pressure transducer signals in the detonation region at $z=5\,\mathrm{mm}$, clearly exhibiting the different number of detonation heads. Key RDE performance numbers evaluated for the time internal [6 ms, 8 ms] are given in Table 3. The reduced back pressure establishes a lower pressure level in the overall chamber, nevertheless the measured detonation velocity of each detonation head in both cases is almost unchanged, remaining at around 60% of D_{CI} . Separate low-resolution simulations have shown that this RDE exhibits detonation velocities close to D_{CI} only for total mass flows of at least $\sim 3\,\mathrm{kg/s}$.

Unrolled slices of pressure, temperature and wall heat flux for the same two time steps as in Fig. 8 are shown in Fig. 10. The top two rows display the pressure and the adaptive mesh in the middle plane at $r=105\,\mathrm{mm}$. The refined mesh is displayed in red while the base mesh is shown in blue. The close approximation of the detonation front region can be clearly inferred. For the time steps shown the case with $p_b=700\,\mathrm{kPa}$ uses $\sim4.95\,\mathrm{M}$ cells on 5698 grids on the refinement level and the case with $p_b=400\,\mathrm{kPa}$ uses $\sim4.98\,\mathrm{M}$ cells on 5078 grids. In the SAMR approach the base level of 1.6 M cells is always integrated in full although at twice as large time steps. Compared to a uniformly refined mesh with 12.8 M cells the savings in computational effort are apparent. While the initial 4 ms take 5.97 h and 5.45 h wall clock time for $p_b=700\,\mathrm{kPa}$ and $p_b=400\,\mathrm{kPa}$, respectively, 47.53 h and 49.75 h are required to complete 52,944 and 58,070 time steps on the finest level to reach the final time $t=8\,\mathrm{ms}$. From the performance of the initial integration to 4 ms one can easily estimate the wall time required to integrate a uniformly refined grid to $t=8\,\mathrm{ms}$ at 98.67 h and 99.82 h, which corresponds to run time savings of 51.8% and 50.2%, respectively.

In the middle of Fig. 10 the temperature at the chamber side walls and in the mid-plane are shown. The simulation with $p_b=700\,\mathrm{kPa}$ shows a more regular RDE combustion and the temperature is therefore more evenly distributed; the average temperature on these three planes is clearly higher. Similar as in Fig. 7, due to the wall cooling, the temperature in the chamber interior is higher. Different to Fig. 7 the injection of the fuel from the outer wall into the air stream does not lead to an even fuel distribution across the chamber width. In these cases, little combustion is occurring near the inner wall and the temperature there stays generally lower. In the bottom graphics of Fig. 10 is shown the wall heat flux as estimated from the wall-normal temperature gradient nearest to the wall. At the inner wall the heat flux for the prescribed wall temperature of 1000 K is close or even below zero. At the outer wall however, in the detonation zone region, values of $> 1.5\,\mathrm{MW}$ are easily reached.

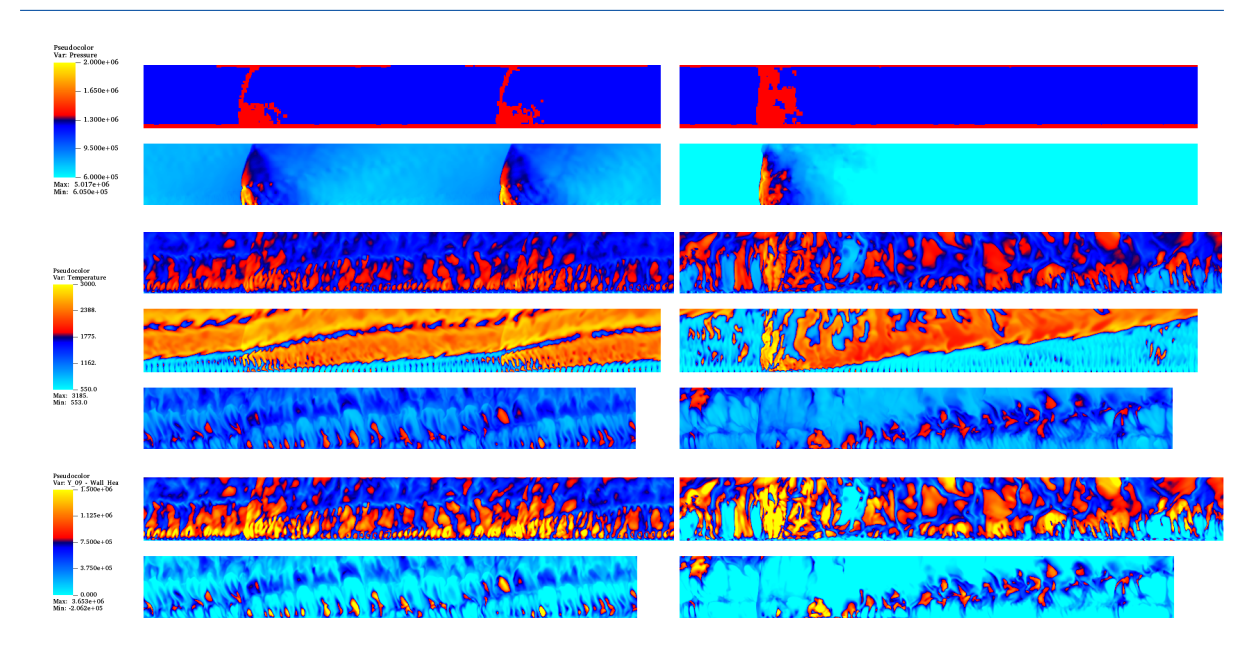


Fig 10. Colour plot on unrolled slices for $p_b = 700 \, \text{kPa}$ at $t = 7.89 \, \text{ms}$ (left) and $p_b = 400 \, \text{kPa}$ at $t = 7.78 \, \text{ms}$ (right). Top: domains of mesh adaptation and static pressure at $r = 105 \, \text{mm}$. Middle: temperature at $r = \{110 \, \text{mm}, 105 \, \text{mm}, 100 \, \text{mm}\}$. Bottom: wall heat flux at $r = \{110 \, \text{mm}, 100 \, \text{mm}\}$.

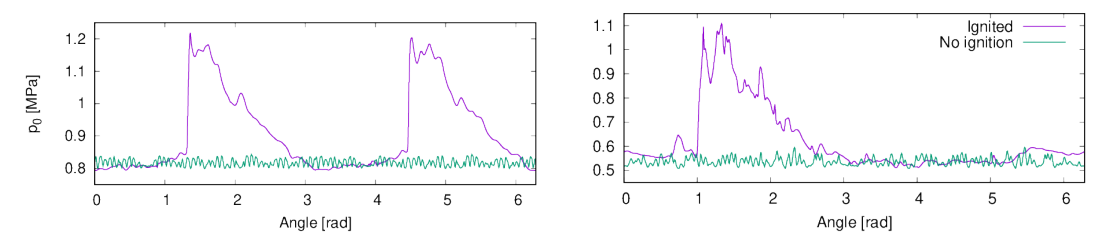


Fig 11. Outlet total pressure p_0 at r = 105 mm for $p_b = 700$ kPa at t = 7.89 ms (left) and $p_b = 400$ kPa at t = 7.78 ms (right) compared to the total pressure at the same location without ignition.

Finally, Fig. 11 displays the total pressure on the middle line $r=105\,\mathrm{mm}$ at the outlet $z=80\,\mathrm{mm}$. Note that at the outlet all values are rather constant in the radial direction from $r=100\,\mathrm{mm}$ to $r=110\,\mathrm{mm}$. The total pressure is evaluated locally in each cell from the standard isentropic relation

$$p_0 = p \left(1 + \frac{\gamma - 1}{2} M^2 \right)^{\frac{\gamma}{\gamma - 1}},$$

where the Mach number M and the adiabatic exponent γ are evaluated for the local mixture and temperature. To enable a direct quantification of the gain in total pressure, two computations have been run in which no initial ZND detonation is present and hence the combustion is not ignited. Figure 11 shows the instantaneous total pressure for the displayed two time steps and a clear gain in total pressure in both RDE simulations is apparent. The right plot of Fig. 11 exhibits that the detonation wave is considerably more perturbed than in the higher back pressure case. The total pressure values in Table 3 have been averaged over the interval $[6\,\mathrm{ms}, 8\,\mathrm{ms}]$. For the higher back pressure RDE case, the spatially averaged values vary between -0.84% and +1.8% around the temporal average of 925.7 kPa, while this configuration without ignition exhibits a variation around the mean of -0.19% and +0.14%. In the lower back pressure case, the spatially averaged total pressure varies by $\pm 4.0\%$ around the temporal mean of 636.5 kPa, while the non-ignited case shows fluctuation from -0.54% + 0.39%. As can be expected, the averaged total pressure gain of the more regularly oscillating high back pressure case is with 108.5 kPa higher than in the low pressure case with 97.8 kPa, although the latter gain appears higher in relative terms with respect to the non-ignited reference. Overall, despite the low value of $\%D_{\mathrm{CJ}}$ both cases clearly exhibit total pressure gain.

5. Conclusions

Numerical simulation is a viable approach to understand the propagation of detonation waves in a rotating detonation engine. The number of parameters influencing in particular the wave count is large and numerical simulations are vitally important to assess design options in advance. We have demonstrated that the detonation solver on curvilinear adaptive meshes in our AMROC framework enables predictive RDE simulations on a moderate number of CPU cores that require a few days of wall clock time each. Using AMROC, we have studied a stoichiometric hydrogen-air RDE with wall cooling and have shown that the average detonation velocity deficit rises only moderately 3.7% to 6.3% when cooling walls are utilized as the wall temperature has a limited effect on the temperature distribution in the middle of the channel. Finally, AMROC has been used to simulate a larger RDE running on stoichiometric ethylene and air. This configuration uses inflow conditions characteristic for an upstream high-pressure compressor and also cooled side walls. It is shown that despite of a considerable detonation velocity deficit, gains in total pressure of 13.3% and 18.1% at the outlet of the RDE combustor are achieved, demonstrating the benefit of the RDE idea. The applied fuel injection pattern of this engine also avoids combustion directly at the inner chamber wall and high wall heat fluxes will have to be mitigated with active cooling only on the outside wall, which will simplify the design considerably.

References

- [1] P. Wolański, "Detonative propulsion," Proc. Combust. Inst., vol. 34, no. 1, pp. 125–158, 2013.
- [2] D. Schwer and K. Kailasanath, "Numerical investigation of the physics of rotating-detonation-engines," *Proceedings of the Combustion Institute*, vol. 33, no. 2, pp. 2195–2202, 2011.
- [3] V. Anand and E. Gutmark, "Rotating detonation combustors and their similarities to rocket instabilities," *Prog. Energy Combust. Sci.*, vol. 73, pp. 182–234, 2019.
- [4] M. Salvadori, A. Panchal, and S. Menon, "Simulation of liquid droplets combustion in a rotating detonation engine," *Proceedings of the Combustion Institute*, vol. 39, no. 3, pp. 3063–3072, 2023.
- [5] H. Peng, C. W. Atkins, and R. Deiterding, "A solver for simulating shock-induced combustion on curvilinear adaptive meshes," *Comput. Fluids*, vol. 232, p. 105188, 2022.
- [6] R. Deiterding, "Block-structured adaptive mesh refinement-theory, implementation and application," in *Esaim: Proceedings*, vol. 34, pp. 97–150, EDP Sciences, 2011.
- [7] H. Peng and R. Deiterding, "A three-dimensional solver for simulating detonation on curvilinear adaptive meshes," *Computer Physics Communications*, vol. 288, p. 108752, 2023.
- [8] B. A. Rankin, D. R. Richardson, A. W. Caswell, A. G. Naples, J. L. Hoke, and F. R. Schauer, "Chemiluminescence imaging of an optically accessible non-premixed rotating detonation engine," Combustion and Flame, vol. 176, pp. 12–22, 2017.
- [9] R. J. Kee, F. M. Rupley, and J. A. Miller, "Chemkin-II: A Fortran chemical kinetics package for the analysis of gas-phase chemical kinetics," tech. rep., Sandia National Lab, Livermore, United States, 1989.
- [10] R. Deiterding, "A parallel adaptive method for simulating shock-induced combustion with detailed chemical kinetics in complex domains," *Computers & Structures*, vol. 87, no. 11-12, pp. 769–783, 2009.
- [11] M. P. Burke, M. Chaos, Y. Ju, F. L. Dryer, and S. J. Klippenstein, "Comprehensive H2/O2 kinetic model for high-pressure combustion," *Int. J. Chem. Kinet.*, vol. 44, pp. 444–474, 2012.
- [12] P. Pal, G. Kumar, S. A. Drennan, B. A. Rankin, and S. Som, "Multidimensional numerical modeling of combustion dynamics in a non-premixed rotating detonation engine with adaptive mesh refinement," *Journal of Energy Resources Technology*, vol. 143, no. 11, 2021.
- [13] D. J. Singh and C. J. Jachimowski, "Quasiglobal reaction mechanism for ethylene combustion," *AIAA Journal*, vol. 31, pp. 213–216, 1994.